






Pressure-induced topological crystalline insulating phase in TlBiSe₂: Experiments and theoryV. Rajaji ^{1,2,3,*},† Raagya Arora ^{1,2,*} B. Joseph ⁴ Subhajit Roychowdhury ^{2,5,6} Umesh V. Waghmare,^{2,7}
Kanishka Biswas,^{2,6} and Chandrabhas Narayana ^{1,2,‡}¹Chemistry and Physics of Materials Unit, Jawaharlal Nehru Centre for Advanced Scientific Research, Jakkur P.O., Bangalore 560 064, India²School of Advanced Materials, Jawaharlal Nehru Centre for Advanced Scientific Research, Jakkur P.O., Bangalore 560 064, India³Univ. Lyon, Université Claude Bernard Lyon 1, CNRS, Institut Lumière Matière, F-69622 Villeurbanne, France⁴Eletra Sincrotrone Trieste, S.S. 14, Km 163.5 in Area Science Park, Basovizza, Trieste 34012, Italy⁵Max Planck Institute for Chemical Physics of Solids, Dresden-01187, Germany⁶New Chemistry Unit, Jawaharlal Nehru Centre for Advanced Scientific Research, Jakkur P.O., Bangalore 560 064, India⁷Theoretical Sciences Unit, Jawaharlal Nehru Centre for Advanced Scientific Research, Jakkur P.O., Bangalore 560 064, India

(Received 18 February 2023; revised 28 April 2023; accepted 2 May 2023; published 22 May 2023)

We report *in situ* high-pressure studies on three-dimensional topological insulator TlBiSe₂ using Raman scattering and synchrotron x-ray-diffraction experiments corroborated with the first-principles theoretical calculations. The phonon modes of a rhombohedral phase of TlBiSe₂ show a systematic increase in frequencies under hydrostatic pressure up to ~ 7.0 GPa. Interestingly, the linewidth of the A_{1g} , N , and E_g phonon modes show clear anomalies at ~ 2.5 GPa which is indicating the isostructural electronic transition. With the help of calculated electron-phonon coupling constant λ , anomalies in the Raman linewidth of E_g mode are attributed to electron-phonon coupling changes. Moreover, our theoretical results reveal that the observed phonon anomalies are due to pressure-induced band inversion at the F points of the Brillouin zone which leads to the changes in electronic topology reflected in the mirror Chern number n_M and \mathbb{Z}_2 topological invariant. Therefore, the phonon anomalies and change in mirror Chern number n_M confirm the pressure-induced topological crystalline insulator phase in TlBiSe₂ at ~ 2.5 GPa. Further, a reversible structural phase transition has been observed above ~ 7.0 GPa from both synchrotron x-ray-diffraction and Raman-scattering measurements. Finally, our studies suggest the use of hydrostatic pressure as a potential pathway for exploring the topological crystalline insulating phase in strong spin-orbit coupling compounds, such as the thallium-based III-V-VI₂ ternary chalcogenide TlBiX₂ ($X = S, Se, Te$) family.

DOI: [10.1103/PhysRevB.107.205139](https://doi.org/10.1103/PhysRevB.107.205139)**I. INTRODUCTION**

The discovery of topological states of quantum matter in three-dimensional (3D) solids had attracted a great deal of scientific interest during the last decade [1,2]. This new kind of quantum matter (topological states) offers potential applications in quantum computations, spintronics, and thermoelectrics. The nontrivial topological materials have a unique electronic band structure which mainly arises due to the strong spin-orbit coupling (SOC). Topological insulator (TI) and topological crystalline insulator (TCI) are the two important topologically nontrivial materials. TIs are a new class of materials that act as bulk insulators, but the surface has conducting (Dirac-like cones in 3D) states [3,4]. These surface-conducting states are protected by time-reversal symmetry and hence cannot be destroyed by nonmagnetic impurities and chemical disorder in the system. Importantly, TI has the odd number of band inversions and is generally characterized by the topological

invariant quantity \mathbb{Z}_2 . TCIs are another interesting class of nontrivial quantum materials, in which an even number of band inversions exist [5,6]. In TCI, the topological states are protected by mirror symmetry rather than time-reversal symmetry (in the case of TIs). Hence, the protection of topological states is not limited by magnetic impurities. Similar to TIs, mirror Chern number n_M is used to characterize the TCI.

It is possible to convert the conventional insulator (trivial insulators) to nontrivial topological insulators (TI and TCI) by tuning the SOC strength in some suitable materials. In the search for new quantum materials, several routes have been proposed for achieving the nontrivial topological phases, both from an experimental and theoretical perspective. For example, the topological states of the materials can be tuned by external perturbations, such as pressure, chemical doping, electric field, etc. [7–10]. Among these, pressure is an ideal tool to induce band inversion (topological states) because of its cleaner and effective nature [11]. The externally applied pressure alters the interatomic bond distances, effective hybridization, decreases the band gap, and consequently induces the topological states in some SOC materials. In fact, hydrostatic pressure-induced TI states have been observed in SOC systems like BiTeI, 1T-TiTe₂, TlBiS₂, BiTeBr, Sb₂Se₃,

*These authors contributed equally to this work.

†rajaji.vincent@univ-lyon1.fr

‡cbhas@jncasr.ac.in

etc. [8,12–15] and pressure-induced TCI states have been witnessed in TlBiS₂ and Cr-doped PbSe (i.e., Pb_{0.99}Cr_{0.01}Se) [13,16].

To probe the topological surface states directly at ambient conditions, surface-sensitive techniques like angle-resolved photoemission spectroscopy (ARPES) can be used [3,4]. Unfortunately, ARPES measurements cannot be performed with materials under high pressure using a diamond-anvil cell (DAC). Hence directly probing the pressure-induced topological states is one of the experimental challenges so far. Here, it is important to mention that during the pressure-induced band inversion, charge-density redistributions and electron-phonon coupling changes occur in the system. Therefore, we can probe the band inversions (topological states) indirectly by measuring the electron-phonon coupling changes. Raman-scattering technique can measure the electron-phonon coupling from phonon linewidth and hence can be used as a potential tool to study the topological transitions [12–14,16–18]. In principle, Raman linewidth is directly proportional to the square of the energy-resolved electron-phonon matrix elements [19] and consequently, it measures the electron-phonon coupling. In fact, the pressure-induced topological states were evidenced by Raman linewidth anomalies (unusual electron-phonon coupling) in various systems such as BiTeI, Sb₂Se₃, 1T-TiTe₂, 1T-TiSe₂, BiTeBr, and TlBiS₂ [12–14,17,20]. Mention must be made that topological transitions in all of these systems were claimed after considering the results of first-principles calculations that show compelling evidence that there is a change in the topological invariant quantities [12–14,18]. Further, we must mention that the various independent high-pressure transport measurements have shown evidence of topological transition that substantiates the claim of Raman linewidth anomalies associated with the band inversion [15,21,22]. It is noteworthy that some of the claimed systems (mentioned above) such as 1T-TiSe₂, TlBiS₂, etc., are yet to be experimentally explored (in the direction of topological transitions) using adequate high-pressure transport techniques.

Thallium-based III-V-VI₂ ternary chalcogenide TlBiX₂ (X = S, Se, Te) are narrow band-gap semiconductors that crystallize in the rhombohedral structure [space group (SG): $R\bar{3}m$] at room temperature [23] and feature a strong SOC. In this family, TlBiTe₂ ($E_g = 0.10$ eV) [24], and TlBiSe₂ ($E_g = 0.28$ eV) [25] are 3D TIs at ambient conditions and are experimentally verified by ARPES [23,26]. TlBiS₂ has a slightly larger band gap ($E_g = 0.40$ eV) [25] and lower SOC strength; therefore, it is not a TI at ambient conditions because the larger band gap and lower SOC avoid the band inversion at ambient conditions. Importantly, TlBiS₂ has a similar electronic and crystal structure as the 3D TIs (TlBiSe₂ and TlBiTe₂) and hence has the possibility of becoming a TI by tuning the SOC strength. In fact, using the two methods (chemical substitutions and high pressure), the TI states are observed in TlBiS₂ at room-temperature conditions. The first one is the partial chemical substitution (chemical pressure) of Se at the S site which leads to the formation of surface states at the Γ point of the Brillouin zone (BZ) [10]. Secondly, the applied hydrostatic pressure induces the TI states in TlBiS₂ at ~ 0.5 GPa [13]. Interestingly, on further increasing the pressure, TlBiS₂ also undergoes the TCI phase at ~ 1.8 GPa

within the stability region of ambient crystal structure (SG: $R\bar{3}m$) [13].

The fascinating observation of the TCI phase in TlBiS₂ creates interest in TlBiSe₂ since TlBiSe₂ shares a similar crystal and electronic structure as TlBiS₂. Due to stronger SOC strength and lower band gap ($E_g = 0.28$ eV), TlBiSe₂ is a 3D TI at ambient conditions [23,26]. Since the crystal structure controls the properties, if we tune the band gap (by high pressure) in TlBiSe₂, then it might have the possibility to become a TCI phase under high pressure like TlBiS₂. Also, recently it was established that there is a strong connection between the enhancement of thermoelectric figure of merit (ZT) and pressure-induced TCI phase transitions [16]. So, the discoveries of the pressure-induced topological phase transitions will be useful for the highly efficient thermoelectrics which are important to produce electricity from waste heat in industrial processes (i.e., green energy-based generators) and also to combat climate change. Furthermore, Raman spectroscopy is a sensitive local technique that can be effectively used for studying the structural, electronic, and topological transitions [12,27]. Hence it will be interesting to investigate the possibility of pressure-induced TCI phase in TlBiSe₂ using Raman-scattering and synchrotron x-ray-diffraction (XRD) measurements and complement with first-principles calculations.

In this present work, we have systematically studied the behavior of 3D TI TlBiSe₂ under hydrostatic compression in a joint experimental and theoretical fashion that combines Raman-scattering and synchrotron XRD experiments and first-principles theoretical calculations. The pressure-induced isostructural electronic transition was observed from the anomalies in Raman linewidth of E_g , N , and A_{1g} phonon modes at ~ 2.5 GPa. First-principles calculations reveal that those anomalies are associated with the TCI phase with the evidence of changes in the mirror Chern number n_M . On further increasing the pressure, a reversible structural phase transition was noticed above 7.0 GPa from both the synchrotron XRD and Raman-scattering measurements.

II. EXPERIMENTAL DETAILS

Polycrystalline samples (~ 1 g) of TlBiSe₂ were synthesized by mixing appropriate ratios of high-purity elemental TI (Aldrich 99.99%), Bi (Aldrich 99.999%), and Se (Alfa Aesar 99.9999%) in quartz tubes. The tubes were sealed under vacuum (10^{-5} Torr) and slowly heated to 723 K over 12 h, then heated up to 1173 K in 4 h, annealed for 10 h, and then slowly cooled down to room temperature over a period of 15 h. The powder XRD experiments of TlBiSe₂ at ambient conditions were recorded using synchrotron radiation with wavelength ($\lambda = 0.4957$ Å) at the Xpress beam line, Elettra synchrotron, Trieste, Italy. The Le Bail method refinement of the obtained XRD pattern confirms the phase identity and purity of the TlBiSe₂.

The Raman-scattering measurements were carried out using the commercial Raman spectrometer LabRAM HR evolution 800 with the wavelength of $\lambda = 633$ nm (HeNe laser). The spectral resolution of the spectrometer is about ~ 0.6 cm⁻¹ for the 150- μ m entrance slit width and the grating of 1800 grooves per millimeter. The *in situ* high-pressure

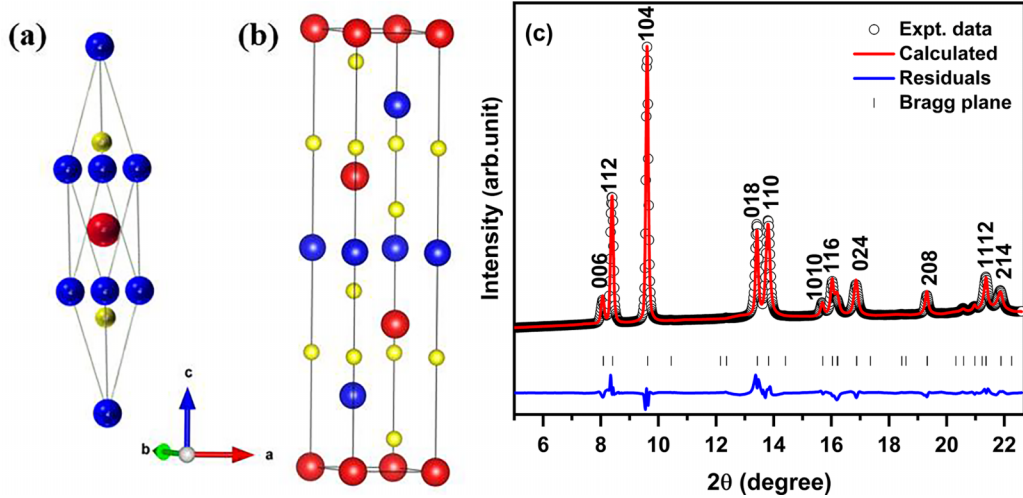


FIG. 1. (a) Schematic of the rhombohedral primitive unit cell, and (b) hexagonal unit cell of TlBiSe_2 . Here, the red, blue, and yellow color spheres represent the Tl^{1+} , Bi^{3+} , and Se^{2-} ions, respectively. (c) Le Bail fit to the synchrotron powder XRD pattern of TlBiSe_2 at ambient conditions.

Raman-scattering measurements were carried out using Mao Bell-type DAC with an anvil culet of 400 μm in diameter. The stainless steel (T301) with starting thickness of $\sim 250 \mu\text{m}$ was used as the gasket material. It was preindented to $\sim 60\text{-}\mu\text{m}$ thickness and the hole in diameter of $\sim 150 \mu\text{m}$ was drilled at the center of the gasket which served as the sample chamber. A mixture of methanol-ethanol in 4:1 ratio was used as the pressure-transmitting medium (PTM), which ensures the hydrostatic condition up to $\sim 10.5 \text{ GPa}$ and quasi-hydrostatic condition up to $\sim 25 \text{ GPa}$ [28]. The *in situ* pressure was calculated by the standard ruby fluorescence method [29]. The typical accumulation time for each of the recorded Raman spectrum is about 15 min. To avoid the risk of laser power-induced damage to the sample, the lower value of laser power ($< 0.5 \text{ mW}$) is kept at the sample.

Synchrotron powder XRD as a function of pressure was carried out at the Xpress beam line, Elettra, Trieste, Italy using a wavelength ($\lambda = 0.4957 \text{ \AA}$). The MAR345 image-plate detector was used. The sample-to-detector distance was calibrated using standard LaB_6 sample and it is found to be 286 mm. The details of gasket preparation, PTM, and pressure calculation are the same as above discussed. The typical accumulation time for each of the recorded XRD pattern is about 10 min. The two-dimensional XRD pattern was converted into 1D pattern (intensity vs 2θ degrees) using FIT2D software [30]. Each XRD pattern was analyzed using FULLPROF software [31].

III. COMPUTATIONAL DETAILS

We performed first-principles theoretical calculations based on the density-functional theory (DFT) by employing the QUANTUM ESPRESSO (QE) code [32]. We used a generalized gradient approximation (GGA) [33] to the exchange-correlation energy with functional parametrized by Perdew, Burke, and Ernzerhof [34]. The projector augmented-wave (PAW) potentials [35] with valence configuration $4f^{14} 6s^2 6p^1 5d^{10}$, $4f^{14} 6s^2 6p^3 5d^{10}$, and $3d^{10} 4s^2 4p^4$ were adopted for Tl, Bi, and Se, respectively. Electronic wave func-

tions and charge density were represented in plane-wave basis sets truncated with cutoff energies of 55 and 550 Ry, respectively. The discontinuity in occupation numbers of electronic states was smeared using a Fermi-Dirac distribution function with the broadening of $k_B T = 0.003 \text{ Ry}$ and integrations over BZ were sampled on a uniform $6 \times 6 \times 6$ mesh of k points in structural relaxation and $12 \times 12 \times 12$ mesh in self-consistent total energy calculations. We used scalar-relativistic PAW potentials to optimize the structure with respect to lattice constants and atomic coordinates, through minimization of enthalpy, $H = E + PV$. Atomic coordinates of thus resulting optimized structures were used as the initial structure in further optimization using fully relativistic potentials; while effects of SOC were included in our calculations of electronic structure through the use of fully relativistic potentials [36], we used scalar-relativistic PAW potentials in the calculation of phonons. Lattice dynamical properties were determined using density-functional linear response (called density-functional perturbation theory (DFPT) [37]) as implemented in the QE package [32]. To obtain phonon dispersion, dynamical matrices were obtained on a $2 \times 2 \times 2$ q -points grid in the BZ. We Fourier interpolated these dynamical matrices to obtain the phonon dispersion along high-symmetry lines (Γ - L - Z - F - Γ - Z) in the BZ. To calculate the bulk electronic topology of TlBiSe_2 , we used the Z2PACK code [38] to determine the \mathbb{Z}_2 topological invariants. This code uses hybrid Wannier functions [39,40] and employs the ideas of time-reversal polarization in the determination of the \mathbb{Z}_2 invariants.

IV. RESULTS

A. Ambient characterization

TlBiSe_2 crystallizes in the rhombohedral crystal structure (D_{3d}^5) at ambient conditions. In this phase, Tl^{1+} , Bi^{3+} , and Se^{2-} atoms occupy $3a$, $3b$, and $6c$ Wyckoff sites, respectively. The fractional coordinates of the Tl, Bi, and Se atoms are (0,0,0.5), (0,0,0), and (0,0,0.2624), respectively. Figures 1(a) and 1(b) represent the schematics of the

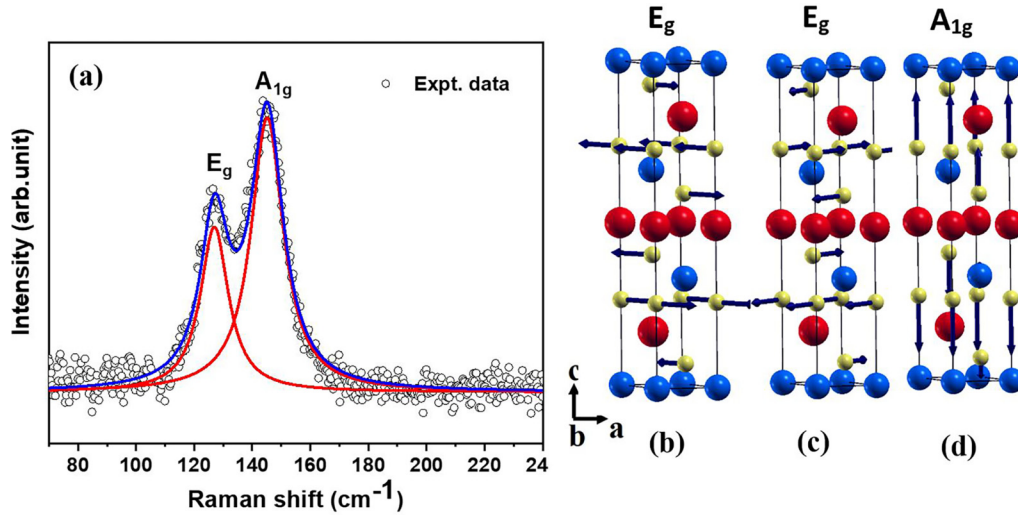


FIG. 2. (a) Experimental Raman spectrum of TlBiSe₂ at ambient conditions. Visualization of the atomic displacements involved in the Raman-active modes (b), (c) E_g and (d) A_{1g} . Here, the red, blue, and yellow colored spheres represent the Tl^{1+} , Bi^{3+} , and Se^{2-} ions, respectively.

rhombohedral primitive unit cell and the hexagonal unit cell of TlBiSe₂, respectively. Figure 1(c) shows the representative synchrotron XRD pattern of TlBiSe₂ at ambient conditions. The calculated lattice parameters from the Le Bail refinement of XRD patterns at ambient conditions are $a = 4.2482 \text{ \AA}$, $c = 22.3019 \text{ \AA}$, and volume $V = 348.57 \text{ \AA}^3$. These calculated values show good agreement with previous reports [41,42].

Group theory-based analysis predicts 12-zone center-phonon modes for the rhombohedral structure of TlBiSe₂ that decompose in the irreducible representations as follows:

$$\Gamma = A_{1g} + 3A_{2u} + 3E_u + E_g.$$

Here, the modes with subscripts g and u represent *gerade* (Raman-active) and *ungerade* modes (infrared (IR)-active), respectively. There are total two Raman-active modes ($A_{1g} + E_g$), four IR-active modes ($2A_{2u} + 2E_u$), and the rest correspond to acoustic phonons ($A_{2u} + E_u$).

Figure 2(a) represents the experimental Raman spectrum of TlBiSe₂ at ambient conditions. We have observed the two Raman modes and are assigned based on our DFT calculations. The Lorentzian function was used to fit the experimental Raman spectrum, and the representative fit is shown in Fig. 2(a). The modes at 127 and 145 cm^{-1} are assigned to E_g and A_{1g} , respectively. The atomic displacement patterns for the E_g and A_{1g} modes are schematically shown in Figs. 2(b)–2(d). The E_g modes represent atomic vibrations of Se atoms in the ab plane, while the A_{1g} modes represent vibrations of Se atoms along the c axis. Table I summarizes the experimental and theoretically calculated Raman frequencies. As evident from

TABLE I. Measured and calculated frequencies of Raman modes for the rhombohedral phase of TlBiSe₂ at $P = 0$ GPa.

Raman mode	Experimental frequency (cm^{-1})	Theoretical frequency (cm^{-1})
E_g	127	126
A_{1g}	145	144

Table I, the calculated Raman-frequency values show good agreement with the experimental values. Further, the calculated phonon dispersion of TlBiSe₂ at ambient conditions is shown in Fig. 3. There are no negative frequencies observed in Fig. 3, thus indicating that the rhombohedral structure is dynamically stable.

B. Synchrotron XRD measurements under pressure

Synchrotron XRD patterns of TlBiSe₂ at selected pressures up to ~ 7.20 GPa are represented in Fig. 4. Upon increasing pressure, the initial rhombohedral structure is stable up to ~ 7 GPa. After that, the appearance of additional Bragg peaks unambiguously identifies the phase transition. Further, it can be observed that the phase transition is fully reversible upon decreasing pressure to ambient conditions. The emphasis of the present work is only on the topological transitions, and therefore the detailed study of this high-pressure structural phase transition is out of the scope. The presence of the strong texture affects the collected XRD patterns and hence limits the full Rietveld refinement. However, we have

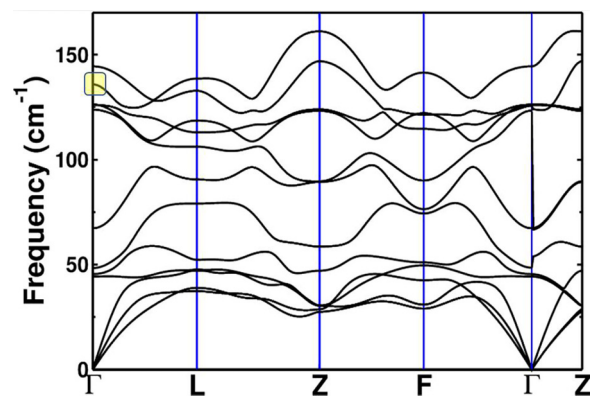


FIG. 3. Calculated phonon dispersion of TlBiSe₂ for theoretical lattice constant at 0 GPa. The absence of negative frequencies indicates that the system is in a stable structure. The yellow color shaded box indicates the location of frequency of the A_{2u} mode.

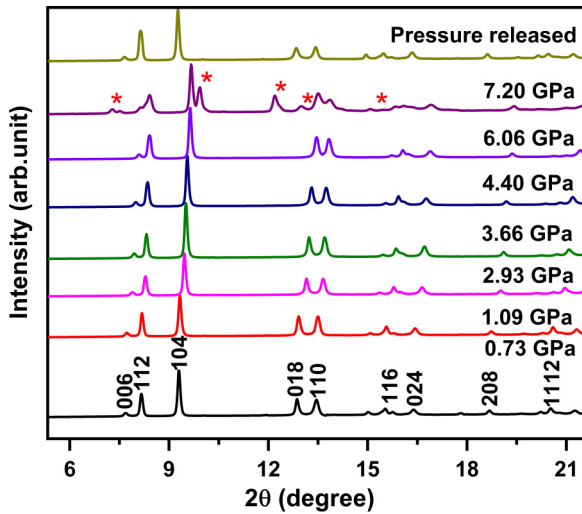


FIG. 4. Pressure evolution of synchrotron XRD patterns of TlBiSe₂ at selected pressure values. Here, the appearance of additional Bragg peaks at high-pressure (~ 7.20 GPa) regions are denoted by the red color asterisk symbol.

analyzed the synchrotron XRD patterns by the Le Bail fit method using FULLPROF software, which estimates the accurate lattice parameters and volume within the permitted error bar. The typical Le Bail fit of the obtained synchrotron patterns at $P = 1.8$ GPa and $P = 5.5$ GPa is shown in Figs. 5(a) and 5(b), respectively (for other pressure values, please see Figs. S1(a) and S1(b) in the Supplemental Material [43]). It is noteworthy that, the fitting parameters of the Le Bail method are not truly significant. Therefore, we did not mention them in Figs. 5(a) and 5(b). Figures 6(a), 6(b), and 6(c) shows the pressure dependence of the unit-cell volume, and lattice parameters a and c , respectively. The pressure vs volume (V) of experimental data was fitted (using EOSFIT 7 software) to a Murnaghan equation of state (EOS) [44] which is given below:

$$P(V) = \frac{B_0}{B'_0} \left[\left(\frac{V_0}{V} \right)^{B'_0} - 1 \right],$$

where V_0 , B_0 , and B'_0 denotes the volume at room pressure, the bulk modulus, and its derivative, respectively. The fit yields $V_0 = 350.00 \text{ \AA}^3$, $B_0 = 35.10$ GPa, and $B'_0 = 4.6$. The obtained value of bulk modulus ($B_0 = 35.10$ GPa) for TlBiSe₂ is slightly lower than TlBiS₂ ($B_0 = 37.65$ GPa) [13]. The pressure dependence of lattice parameters (a and c) fitted (using EOSFIT 7 software) to a Murnaghan EOS yields the linear compressibility of a axis K_a (or K_b) = $8.32 \times 10^{-3} \text{ GPa}^{-1}$ and that of c axis, $K_c = 14.30 \times 10^{-3} \text{ GPa}^{-1}$. Furthermore, the c/a ratio decreases monotonically with hydrostatic pressure, as shown in Fig. 6(d). Here, it can be noted that lattice parameters (a and c) and the axial ratio (c/a) do not show any anomalies within the experimental resolution.

C. Raman-scattering measurements under pressure

Figure 7(a) represents the pressure dependence of the Raman spectrum of TlBiSe₂ up to ~ 7.30 GPa. Upon increasing

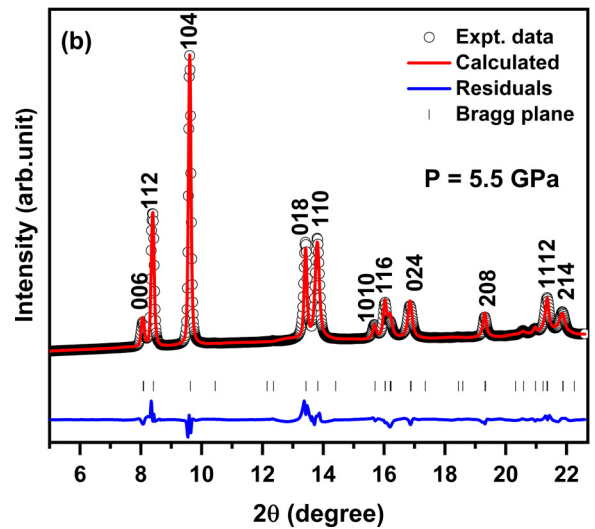
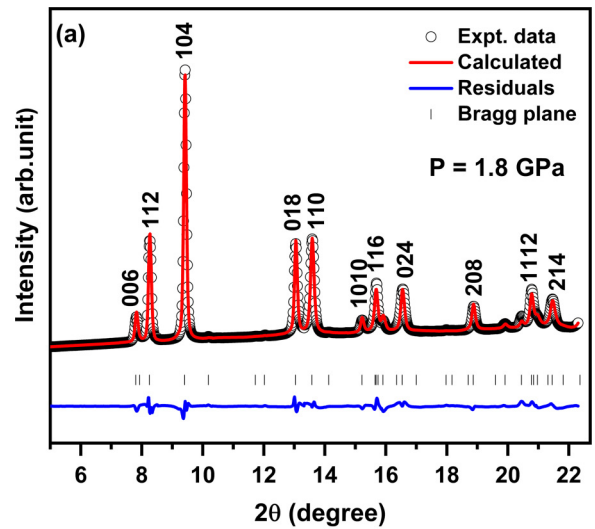


FIG. 5. Le Bail fit to the synchrotron XRD patterns of TlBiSe₂ at (a) $P = 1.8$ GPa and (b) $P = 5.5$ GPa. Wavelength $\lambda = 0.4957 \text{ \AA}$ was used for the high-pressure XRD experiments.

pressure, four major changes are noticed in the Raman spectra. (i) The appearance of additional Raman modes above ~ 7.0 GPa confirms the structural phase transition which is consistent with the synchrotron high-pressure XRD measurements. (ii) The intensity of A_{1g} peak decreases and eventually disappears at close to phase transition pressure (~ 7.0 GPa). (iii) The intensity of E_g peak monotonically increases with pressure. (iv) A peak (named as N) started to appear at ~ 1.0 GPa within the experimental resolution and also evolves systematically (becoming a sharper peak in nature) with respect to increasing further pressure. Here, it is important to discuss the possible origin of this peak N . As the incident laser power at the sample is very less (< 0.5 mW), power density will not generate huge temperatures. Therefore, the appearance of the N peak could not be due to laser heating. Another possibility is the splitting of the doubly degenerate mode E_g under pressure. But, the separation between the E_g and N peak is large (for instance, around 10 cm^{-1} at 1.0 GPa), and also the absolute intensities of these two modes are different. Moreover, our pressure dependence of the phonon calculation

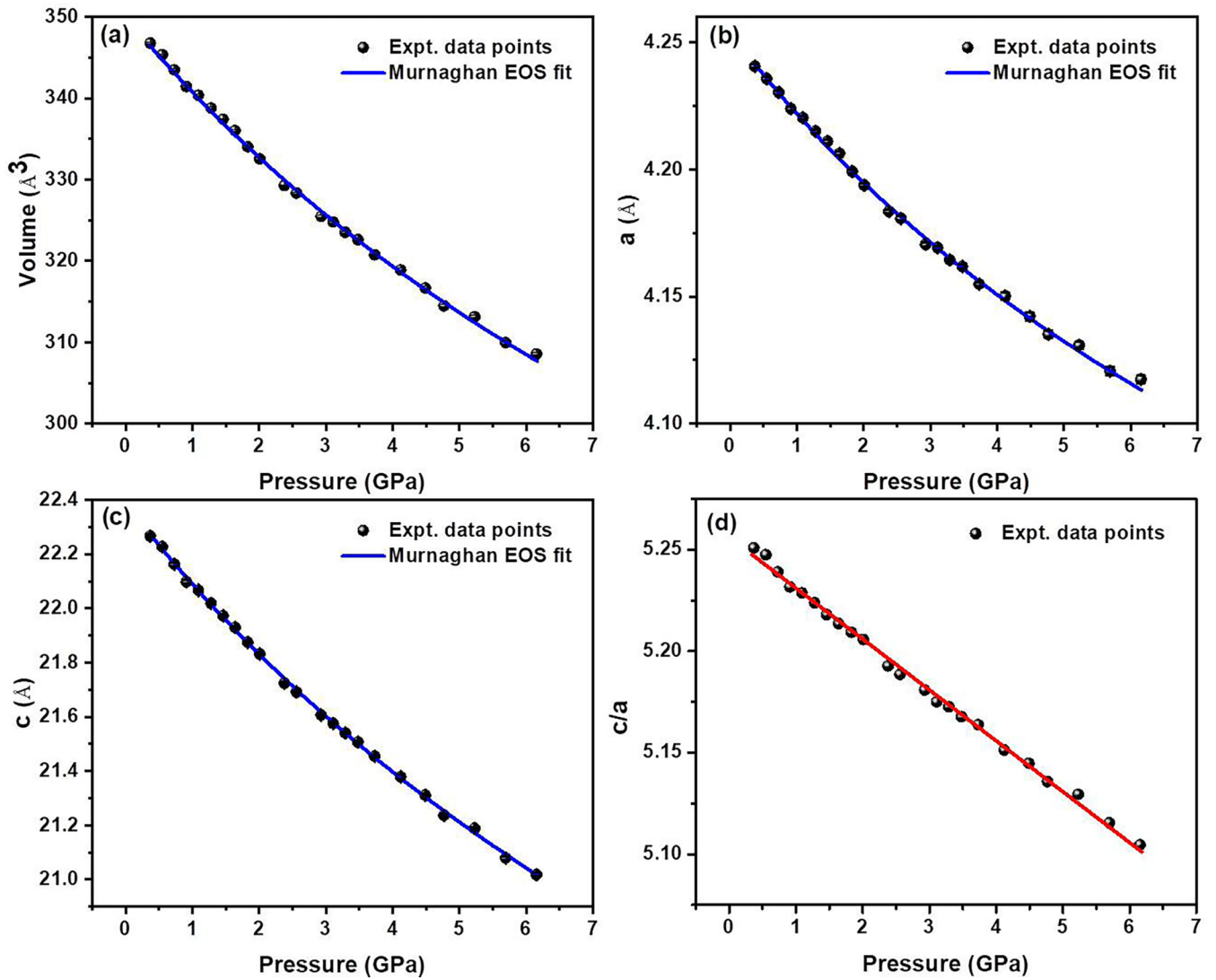


FIG. 6. (a) Pressure dependence of the unit-cell volume (V), lattice parameters (b) a , (c) c , and (d) c/a ratio of the rhombohedral phase of TlBiSe₂. Blue and red solid lines represent the Murnaghan EOS fit and a guide to the eye, respectively.

does not evidence the degeneracy splitting of E_g mode. Hence, the possibilities of degeneracy splitting are ruled out. In addition, our synchrotron XRD measurements on TlBiSe₂ revealed that the pressure-induced structural transition occurs only at ~ 7.0 GPa, and hence this N peak cannot be associated with a high-pressure phase. Interestingly, our DFPT-based calculations revealed that the frequency of A_{2u} mode is closely matching with that of the N mode.

In specific, we observed that approaching the Γ point along the ΓL direction (highlighted in yellow in Fig. 3) results in a close match between the frequency of the A_{2u} mode and that of the N -mode frequency (135 cm^{-1}). However, when approaching the Γ point along the ΓZ or ΓF direction, we observed a lower frequency of the A_{2u} mode at 125 cm^{-1} (see in Fig. 3). This phenomenon is due to the long-range Coulomb interaction in polar materials, which makes the dynamical matrix nonanalytical in the $q \rightarrow 0$ limit and leads to the LO-TO splitting. For instance, similar to our case, the splitting of LO and TO components was observed in wurtzite $\text{Al}_x\text{Ga}_{1-x}\text{N}$ alloys [45]. Further, using group theory analysis [46], the

A_{2u} mode is identified as the hyper-Raman-active mode and hence it is possibly detected in experiments. Additionally, DFT-calculated structural parameters evidence the prominent change in slope of the Tl-Se bond length [see Fig. 9(a)], and the u parameter [see Fig. 9(b)] with pressure at $P_c \sim 2.5\text{--}3.0$ GPa, signifying the possibility of an isostructural transition seen in our experimental observations. These minor changes might play a role in enhancing the detection of the N mode at ~ 1.0 GPa in experiments. In summary, to give clear experimental insight into this interesting Raman mode (N) (hyper-Raman mode A_{2u}), the polarization-dependent behavior of this mode in the single-crystalline sample is required, which is the subject of our future interest. The additional discussion about the detection of hyper-Raman-active mode and disordered structures with relevant examples in the literature [47–51] is commented upon in the Supplemental Material [43].

To get more details, we have plotted pressure vs Raman shift of various phonon modes of TlBiSe₂ up to ~ 7.0 GPa as shown in Fig. 7(b). The representative Lorentzian fitting to

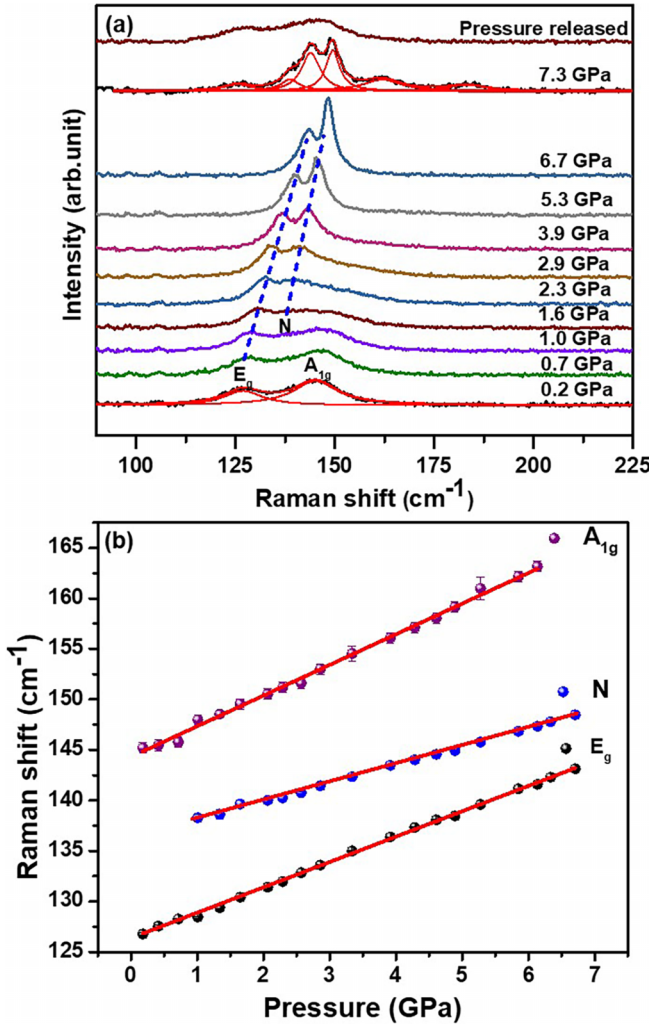


FIG. 7. (a) Pressure evolution of the Raman spectra of TlBiSe₂ at various selected pressures up to ~ 7.3 GPa. Blue dotted line represents a guide to the eye. (b) Pressure dependence of the Raman shift of A_{1g} , E_g , and N phonon modes up to $P \sim 7.0$ GPa. Red solid line represents a linear fit to the experimental data.

the experimental Raman spectrum for the selected pressure values is shown in Figs. S2(a)–S2(d) [43]. As evident from Fig. 7(b), the phonon-mode frequencies of E_g , N , and A_{1g} monotonically increase up to ~ 7.0 GPa without any changes (within the experimental resolution). In fact, this is the general expected trend (hardening) for any phonon mode with applied pressure. The pressure-dependence behavior of all these Raman modes (E_g , N , and A_{1g}) is fitted using a linear equation up to ~ 7.0 GPa. Table II summarizes the fitting parameters (pressure coefficients) and Gruneisen parameters of various Raman modes. As evident from Table II, the pressure coefficient (a_1) of the E_g mode ($2.51 \text{ cm}^{-1} \text{ GPa}^{-1}$) is smaller than the A_{1g} mode ($3.04 \text{ cm}^{-1} \text{ GPa}^{-1}$). The pressure coefficient of E_g and A_{1g} mode is directly related to the compressibility of the lattice parameters a and c , respectively. From our synchrotron XRD results, the compressibility of the c axis is greater than the a axis, which is consistent with Raman data of pressure coefficients of E_g and A_{1g} modes.

Raman spectroscopy can be effectively used for studying the various fundamental interactions existing in the

TABLE II. Pressure-dependence behavior of various first-order Raman-mode frequencies and Gruneisen parameters (γ) of TlBiSe₂. Pressure coefficients for TlBiSe₂ were fitted using the linear equation $\omega(P) = \omega(P_0) + a_1(P - P_0)$. Gruneisen parameters γ are determined by using the relation $\gamma = (\frac{B}{\omega(P_0)} \times \frac{\partial \omega}{\partial P})$, where B represents the bulk modulus ($B_0 = 35.10$ GPa).

Raman mode	$\omega(P_0)$ (cm^{-1})	a_1 ($\text{cm}^{-1} \text{ GPa}^{-1}$)	γ
E_g	126.4 ± 0.1^a	2.51 ± 0.02^a	0.70
N	136.1 ± 0.1^a	1.84 ± 0.02^a	0.47
A_{1g}	144.3 ± 0.1^a	3.04 ± 0.04^a	0.74

^aEstimated at room pressure ($P_0 = 1$ atm).

solid system. Precisely, Raman linewidth is inversely proportional to phonon lifetime for the crystalline materials. Hence, it could provide information about the phonon-phonon interactions, electron-phonon coupling, and spin-phonon coupling existing in the system [14,17,52,53]. Therefore, we have carefully analyzed the linewidth [i.e., full width at half maximum (FWHM)] of the phonon modes, and they are represented in Figs. 8(a) and 8(b). In general, upon increasing pressure, a systematic increase in linewidth of phonon modes should be expected. However, here the FWHM of the E_g decreases under pressure up to ~ 2.5 GPa, and then shows almost constant behavior within the experimental resolution. The linewidth of N mode decreases up to ~ 7.0 GPa with a significant slope change at 2.5 GPa. The FWHM of the A_{1g} peak increases upon pressure up to ~ 6.1 GPa with a clear slope change at 2.5 GPa. Interestingly, the observed anomalies in the linewidth of various phonon modes at ~ 2.5 GPa might indicate the unusual electron-phonon coupling that possibly arises from the changes in the electronic band structure at high pressure. It is noteworthy that the PTM also contributes to linewidth changes beyond its hydrostatic limit. Here, the used PTM [methanol:ethanol (4:1) mixture] gives the hydrostatic limit up to ~ 10.5 GPa and hence clearly rules out the PTM contribution and ascertains that changes observed are intrinsic to the sample. Since TlBiSe₂ undergoes a structural phase transition (both in synchrotron high-pressure XRD and high-pressure Raman-scattering experiments) only at ~ 7.0 GPa, the observed phonon anomalies in our experiments cannot be due to a structural phase transition. Therefore, the observed phonon anomalies at ~ 2.5 GPa clearly suggest an isostructural electronic transition in TlBiSe₂.

D. Theoretical calculations

To understand the experimentally observed Raman anomalies (isostructural electronic transition) at ~ 2.5 GPa, we used first-principles calculations to simulate the rhombohedral phase of TlBiSe₂ as a function of pressure. Our estimates of optimized lattice constants of TlBiSe₂ are $a = b = 4.29 \text{ \AA}$, and $c = 22.7 \text{ \AA}$, which agree within the typical GGA errors with their experimental values ($a = b = 4.24 \text{ \AA}$, $c = 22.30 \text{ \AA}$). Lattice parameters of TlBiSe₂ vary smoothly with hydrostatic pressure, signifying the robustness of its crystal structure up to $P \sim 7.0$ GPa. Variation in calculated lattice parameters (a and c) with pressure [Fig. S3(c)] shows that compression of the c axis is notably faster than that for the

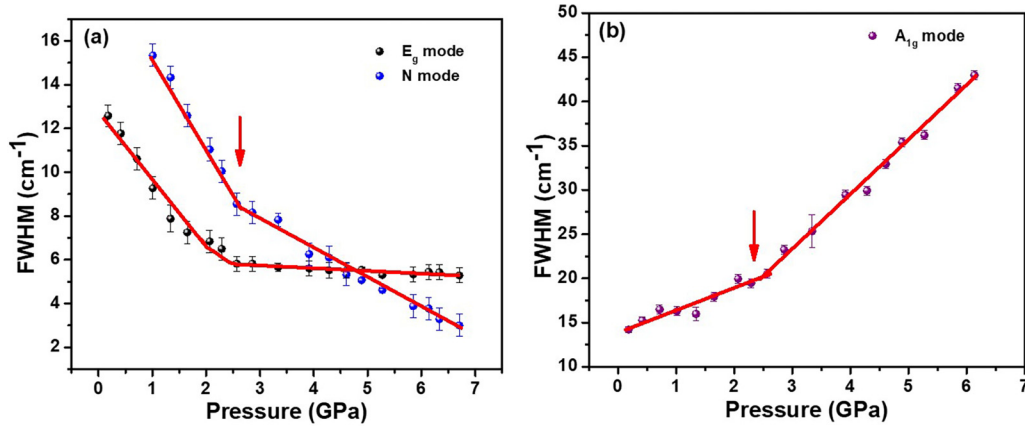


FIG. 8. (a) Pressure dependence of FWHM of E_g and N modes for TlBiSe_2 . (b) Pressure vs FWHM of A_{1g} mode. Solid red arrows at ~ 2.5 GPa indicate the isostructural electronic transition. Red solid lines represent a guide to the eye.

a axis in corroboration with our experimental observations. In addition, variation in the Tl–Se bond lengths with pressure [Fig. 9(a)] shows changes in the slope with pressure at $P_c \sim 2.5$ GPa supporting the isostructural phase transition seen in our experimental observations. Here, it is worth monitoring the positions of Se atoms with pressure; only the z coordinate of Se position (z –Se; u) defines the Wyckoff positions that are allowed to vary (Tl, and Bi atoms are fixed). There is a prominent change in the slope of the u parameter with pressure at $P_c \sim 3$ GPa, signifying a possibility of an isostructural phase transition [Fig. 9(b)].

We now attempt to uncover the possible origin of pressure-dependent changes in Raman anomalies with the electronic band structure analysis. The electronic structure of TlBiSe_2 calculated including SOC at the optimized lattice constants ($P = 0$ GPa) reveals a direct band gap of 0.16 eV at the F point. The band gap estimated here is slightly lower than the experimental band gap of 0.28 eV, which is typical of DFT calculations to underestimate band gaps. The electronic structure of TlBiSe_2 exhibits valleys at the Γ and F points of the BZ. Band gaps estimated using optimized lattice constants (ambient pressure) at Γ and F points are 0.31 and 0.16 eV, respectively [see Fig. 10(b)]. With increasing pressure from 0 to 4 GPa, the energy gap at the F point first closes and then reopens close to P_c^F between 1 and 2 GPa [see Fig. 10(f)]. A

close examination of the electronic structure at the F point reveals the inversion of valence- and conduction bands as pressure increases from 1 to 2 GPa; it is further evident in the isosurfaces of charge densities [Fig. 11(a)] associated with these bands.

On the other hand, the band gap at Γ point increases monotonously with increasing hydrostatic pressure from 0 to 7 GPa, and the gap separating the valence and conduction bands at Γ point reduces with negative hydrostatic pressure. The band gap reduces from 0.31 eV at 0 GPa to 0.10 eV at -2 GPa [Fig. 10(f)] and then opens up with further negative pressure. Electronic structure at Γ reveals an inversion of valence and conduction bands at P_c^Γ in between $P = -2$ and -3 GPa, which is also evident in the isosurfaces of charge densities [Fig. 11(b)] associated with these bands. Furthermore, to understand the effect of SOC in TlBiSe_2 , we have calculated the electronic band structure of TlBiSe_2 without SOC, and the results are shown in Fig. S4 and commented upon in Supplemental Material [43].

V. DISCUSSION

Band inversion is one of the signatures of topological quantum-phase transitions (TQPT) [1,14,18] and hence motivates us to examine the pressure-dependent bulk electronic

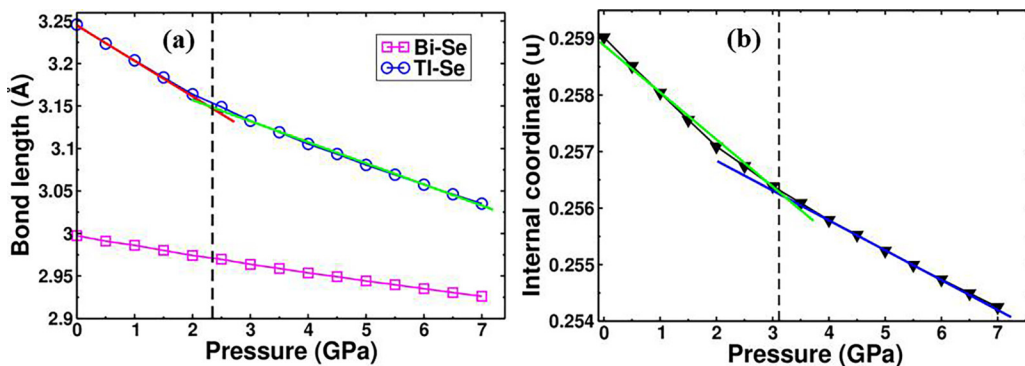


FIG. 9. (a) Calculated pressure dependence of Bi–Se and Tl–Se bond lengths, and (b) the position of Se atoms (internal coordinate) in the rhombohedral phase of TlBiSe_2 . Here, the pressure dependence of these structural parameters exhibits changes in the slope at around $P = 2.5$ – 3.0 GPa.

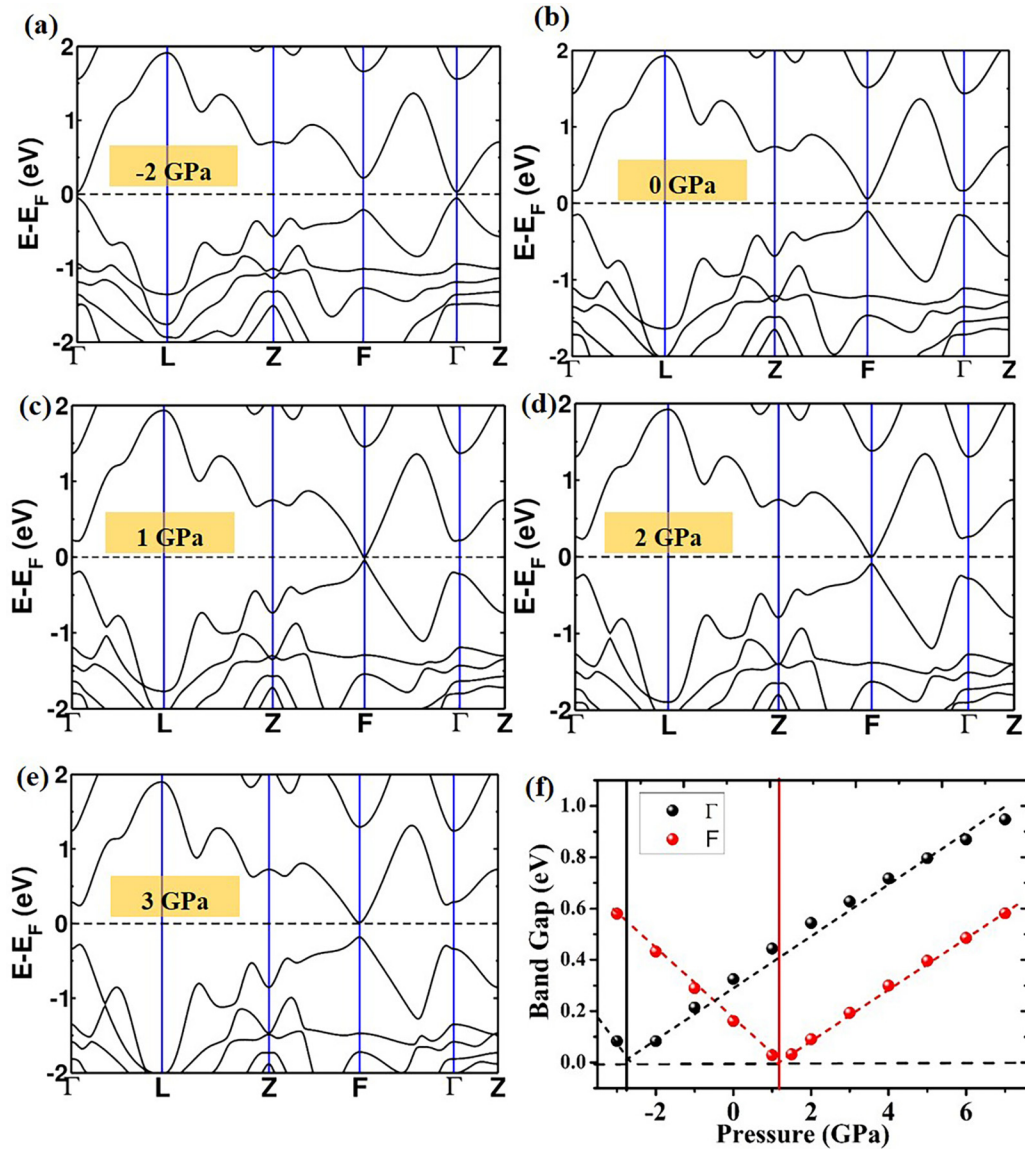


FIG. 10. (a)–(e) Electronic structure of TlBiSe₂ calculated with the inclusion of SOC at different hydrostatic pressures (in the range $P = -2$ to 3 GPa). (f) Evolution of direct band gaps at Γ and F points with hydrostatic pressure showing opening and closing of gaps at the critical pressures (P_C^F and P_C^Γ). Dashed lines represent a guide to the eye.

topology of TlBiSe₂. To confirm its topological insulating character, we determined the strong \mathbb{Z}_2 topological index using a robust and exact method as employed in the Z2PACK code [38]. The strong \mathbb{Z}_2 topological invariant (ν_0) of TlBiSe₂ calculated at 0 GPa is $\nu_0 = 1$ (TI). Thus, the \mathbb{Z}_2 topological index confirms the nontrivial band topology of TlBiSe₂ at ambient pressures and is consistent with the experimental observation of ARPES measurements [23,26]. Further, the calculated \mathbb{Z}_2 at 1 and 2 GPa is $\nu_0 = 1$ (TI) and $\nu_0 = 0$ (normal insulator), respectively, confirming the change in electronic topology, and establishing the trivial band topology of TlBiSe₂ at pressures greater than $P_C^F > 1$ GPa. We find that the topological invariants calculated at -3 , -2 , -1 , and 0 GPa ($\nu_0 = 0, 1, 1$, and 1, respectively) reveal another low-pressure TQPT at critical pressure (P_C^Γ) between -2 and -3 GPa.

An even number of band inversions typically leads to a TCI phase. In TlBiSe₂, the band gap closes and reopens through an

even number of inversions between the two extreme pressures (-3 and 2 GPa), implying that even though the phase above 1 GPa cannot be a \mathbb{Z}_2 TI, we can obtain a TCI phase driven by the mirror symmetry of the hexagonal lattice. To this end, we determined the mirror Chern number (n_M) as a function of pressure. The calculated mirror Chern numbers (n_M) of TlBiSe₂ at $P = 1$ and 2 GPa are $n_M = 1$ and $n_M = 2$ (TCI), respectively. Thus, n_M confirms the change in electronic topology and establishes the nontrivial crystalline topology of TlBiSe₂ and the TCI phase at pressures above 1 GPa. The experimentally observed anomalies in phonon linewidths of A_{1g} , E_g , and N modes at $P \sim 2.5$ GPa are closely consistent with our theoretical prediction. Hence, we can attribute the observed isostructural electronic transition in TlBiSe₂ at ~ 2.5 GPa to TCI transition accompanied by the n_M .

Notably, a small difference in the transition pressures obtained from an experiment (~ 2.5 GPa) and theory (~ 1.2 GPa)

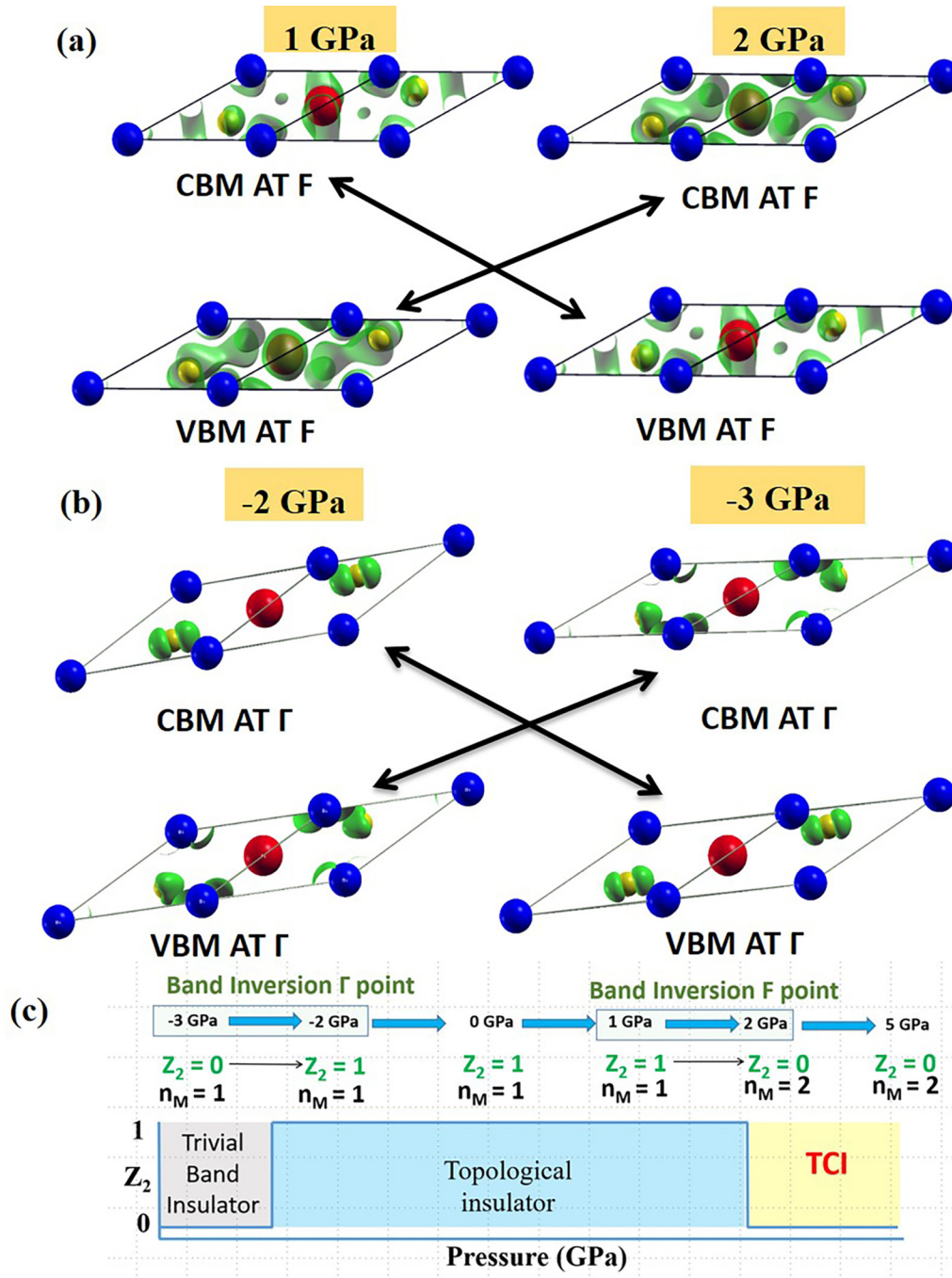


FIG. 11. Inversion of bands at the transition pressures, visualized with isosurfaces of charge densities of states at the valence-band maximum (VBM) and conduction-band minimum (CBM) at (a) F point takes place between 1 and 2 GPa (i.e., $1 < P_C^F < 2$ GPa at F point) and (b) Γ point takes place between -2 and -3 GPa (i.e., $-3 < P_C^\Gamma < -2$ GPa at F point). (c) Z_2 topological invariant and mirror Chern number n_M of TlBiSe_2 evaluated as a function of hydrostatic pressure. Here, the red, blue, and yellow color spheres represent the Tl^{1+} , Bi^{3+} , and Se^{2-} ions, respectively.

is observed. Generally, the DFT theory involves various approximations and shows the typical error in various critical parameters such as calculated band gaps, lattice parameters, and unit-cell volume. Therefore, the transition pressure from DFT results may not quantitatively match with high-pressure experiments. For example, the TQPT was predicted in BiTeI at 1.7 and 4.1 GPa using the local-density approximations and GGA, respectively [7], while the experimentally explored transition pressure is ~ 2.0 – 2.9 GPa [8]. Similarly,

the TCI transition is predicted at $P \sim 3.6$ GPa in TlBiS_2 system using GGA approximations [13]. However, the experimentally observed transition pressure is $P \sim 1.8$ GPa [13]. These examples clearly demonstrate the common observation of a mismatch of transition-pressure values between the high-pressure experiments and DFT calculations. However, most importantly, we have observed an isostructural electronic transition from the Raman linewidth anomalies at ~ 2.5 GPa within the stability of the rhombohedral structure

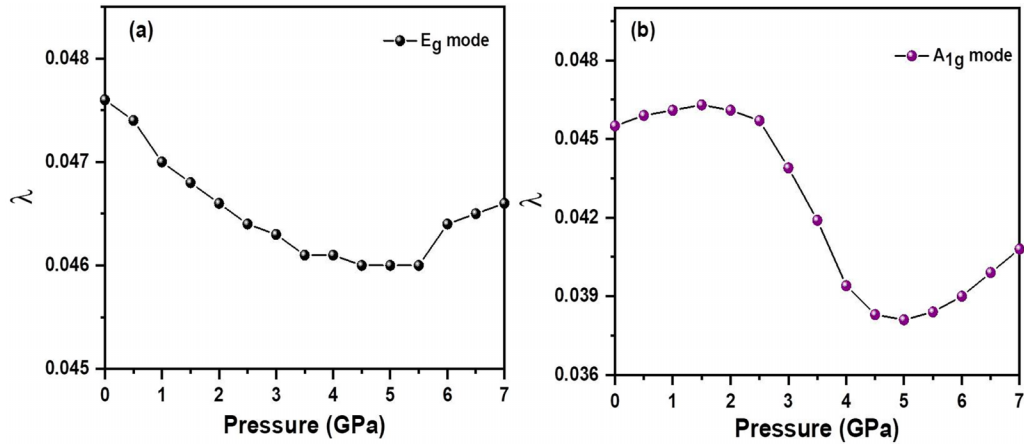


FIG. 12. Changes in the DFT-calculated electron-phonon coupling constant λ of Raman-active, (a) E_g , and (b) A_{1g} modes of TlBiSe_2 with pressure (from 0 to 7.0 GPa).

of TlBiSe_2 , and our DFT calculations confirm the presence of TCI transition with the evidence of mirror Chern number n_M at ~ 1.2 GPa quite close accurately.

Pressure dependence of both the Raman-active phonon modes (calculated) is shown in Figs. S5(a) and S5(b) [43]. Calculated frequencies of Raman-active phonon modes (A_{1g} and E_g) exhibit systematic hardening with increasing pressure, which is in good agreement with experimental observations. The measure of electron-phonon interaction is the electron-phonon coupling constant λ , which is directly proportional to the Raman linewidth [13,18,54]. Therefore, we have calculated the pressure dependence of λ for both the E_g and A_{1g} modes. The calculated λ [see Fig. 12(a)] of E_g mode shows the systematic trend of reduction and then a slight rise, closely consistent with the observed behavior of linewidth of E_g mode [see Fig. 8(a)]. Therefore, changes in the Raman linewidth of E_g mode are attributed to electron-phonon coupling changes. Thus, there is a clear correlation between changes in the behavior of Raman-active mode E_g as a function of pressure, and TQPT recorded within our theoretical analysis. Furthermore, it is important to mention that, upon pressure, decreasing linewidth of phonon mode E_g and changes in the calculated electron-phonon coupling constant λ have been observed for the TlBiSe_2 compound [13] during topological transitions.

As regards A_{1g} mode, the calculated λ [see Fig. 12(b)] slightly increases up to ~ 2.0 GPa and then undergoes a drastic reduction until ~ 5.0 GPa. Afterward, λ again slightly increases with increasing pressure. But, experimentally, as the pressure increases, FWHM of the A_{1g} peak increases with a distinct slope change at 2.5 GPa [see Fig. 8(b)]. Therefore, the pressure dependence of calculated λ and experimental FWHM for A_{1g} mode is not similar. However, the trend of change in slope near low pressure of ~ 2.0 GPa in A_{1g} mode is correctly captured in our calculated λ , hinting toward topological transition. In general, the Raman linewidth (FWHM) for the crystalline material contains the major contribution from electron-phonon interactions and anharmonic phonon-phonon interactions. Therefore, the possible mismatch between the experimental FWHM and theoretically calculated λ might suggest the existence of strong phonon-phonon coupling in A_{1g} mode upon increasing pressure. To support this, very

recently the strong anharmonic phonon-phonon coupling existence was observed in the TlBiSe_2 compound [55] and hence it can be one critical factor. Furthermore, here we want to highlight that some high-pressure calculations present similar noncorrelated phonon linewidth behaviors with the experiments. For instance, phonon modes A_g^1 and A_g^2 of black phosphorus compound exhibit the anomalies in calculated λ during the topological transitions under high pressure and are consistent with experimental results [18]. But, the pressure dependence of phonon mode B_{2g} of black phosphorus shows different behavior of λ compared to its experimental FWHM [18]. Moreover, the choice of exchange-correlation functional can significantly affect the accuracy of the results in DFT calculations and therefore it is another critical factor. For instance, the accuracy of the calculated electron-phonon coupling constant λ can be improved by using a more advanced functional, such as the screened-exchange hybrid functional [56]. In summary, to address the more accurate pressure dependence of Raman linewidth anomalies in A_{1g} mode for the TlBiSe_2 compound, anharmonic approximations and screened-exchange hybrid functional should be included but is computationally expensive and beyond the scope of the present work.

Now it is interesting to compare high-pressure behavior across ternary chalcogenide TlBiX_2 ($X = \text{S, Se, Te}$) systems. The present result is consistent with our earlier work on the pressure-dependent study of TlBiS_2 where Raman anomalies were observed at ~ 0.5 and ~ 1.8 GPa and corresponding first-principles DFT calculated critical pressures of ~ -0.4 and ~ 3.6 GPa were attributed to nontrivial TQPT transitions [13]. In addition, we also examined the pressure-dependent electronic structure and topological invariants \mathbb{Z}_2 and n_M of TlBiTe_2 . The hydrostatic pressure-dependent electronic structure of TlBiTe_2 was calculated without and with including the SOC at different hydrostatic pressures (from -2 to 8 GPa) and the results are shown in Fig. S6 and Fig. S7, respectively. We find a low-pressure TQPT from a normal insulator to a strong TI at the critical pressure (P_C^I) between -2 GPa ($\nu_0 = 0$) and -3 GPa ($\nu_0 = 1$) associated with the opening and closing of the band gap at Γ . A second band inversion at F results at another topological

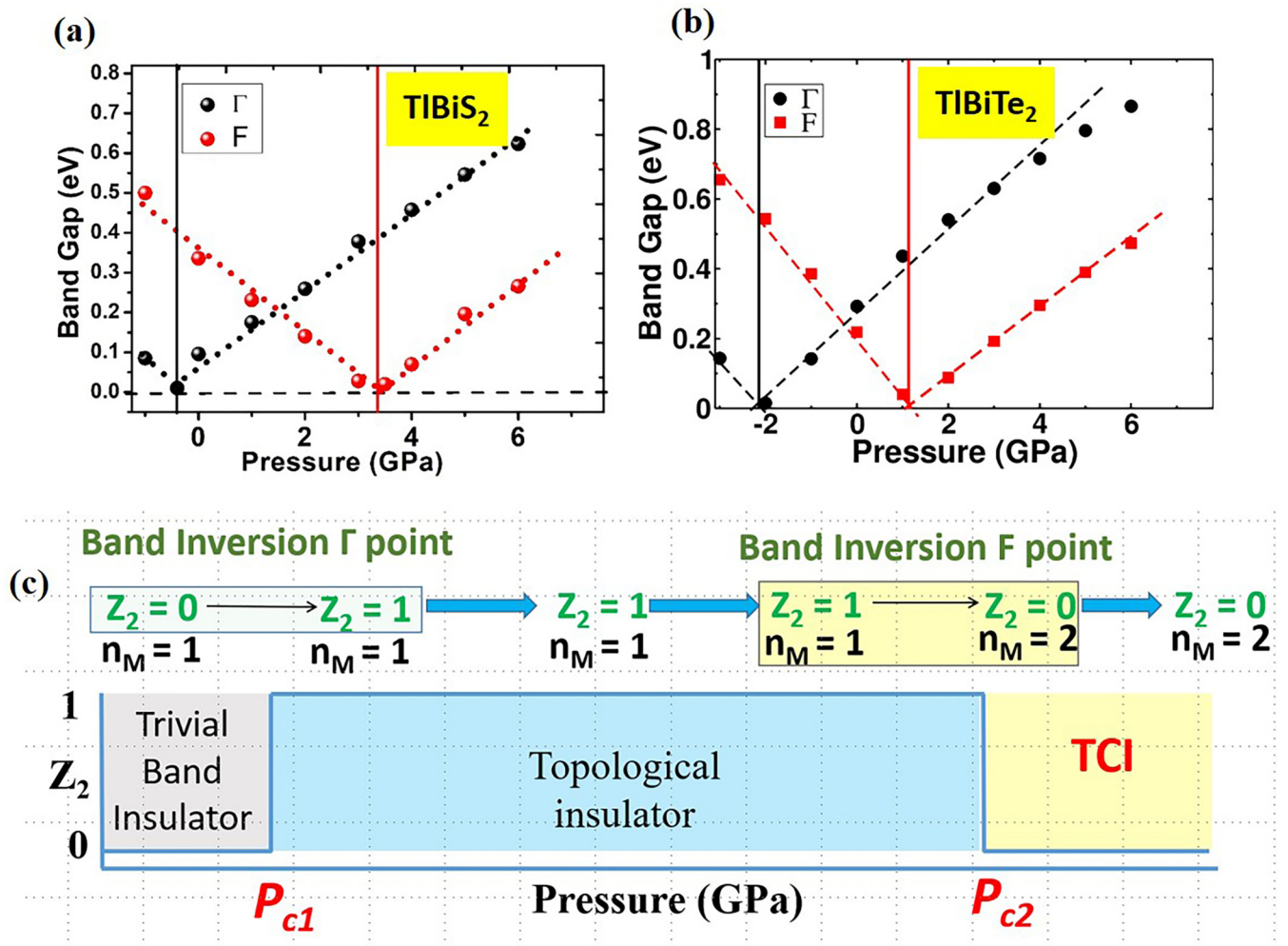


FIG. 13. General features of pressure-dependent TQPT in TIBiX_2 ($X = \text{S, Se, Te}$) family. Evolution of band gaps at Γ and F points with hydrostatic pressure reveals band inversions in (a) TIBiS_2 (adopted from Ref. [13]) and (b) TIBiTe_2 at the critical pressures (P_{c1}^F and P_{c1}^Γ). (c) \mathbb{Z}_2 topological index and mirror Chern number n_M of TIBiX_2 ($X = \text{S, Se, Te}$) evaluated as a function of hydrostatic pressure.

phase transition from strong TI to a TCI at the critical pressure (P_{c1}^F) between 1 GPa ($\nu_0 = 1, n_M = 1$) and 2 GPa ($\nu_0 = 0, n_M = 2$). The evolution of band gap at Γ and F points with hydrostatic pressure shows band inversion at the critical pressures (P_{c1}^Γ and P_{c1}^F) of TIBiX_2 ($=\text{S, Se, Te}$), and comparison between invariant quantities \mathbb{Z}_2 and n_M are shown in the schematic in Fig. 13. In summary, our first-principles calculations show that there are two pressure-dependent TQPTs in TIBiX_2 ($X = \text{S, Se, Te}$). (i) An odd number of inversions occurring at Γ point results in the change of \mathbb{Z}_2 topological invariant from 0 (normal insulator) to 1 (strong \mathbb{Z}_2 TI) at critical pressure P_{c1}^Γ [between -3 and -2 GPa in $\text{TIBiSe}_2/\text{TIBiTe}_2$ and between -1 and 0 GPa in TIBiS_2]. (ii) The second band inversion is noticed at F point with critical pressure (P_{c1}^F) [between 1 and 2 GPa for $\text{TIBiSe}_2/\text{TIBiTe}_2$ and between 3 and 4 GPa for TIBiS_2]. Therefore, an overall even number of inversions (3 from F and 1 from Γ) results in $n_M = 2$ (TCI state) and \mathbb{Z}_2 topological index 0.

The experimentally explored high-pressure TCI transition in the TIBiSe_2 compound can be observed at room temperature by chemical pressure strategy. For instance, the chemical substitution of Sn in the binary chalcogenide PbSe system

(i.e., $\text{Pb}_{1-x}\text{Sn}_x\text{Se}$) leads to the formation of a TCI state at $x = 0.23$ at ambient conditions [9]. Similarly, ternary chalcogenide $\text{TIBi}(\text{S}_{1-x}\text{Se}_x)_2$ gives the TI state at $x \sim 5\%$ at ambient conditions [10]. Therefore these examples clearly illustrate that the chemical method is one of the promising routes to observe the explored TCI in TIBiSe_2 at ambient conditions. Importantly, TCI transition has been shown to enhance thermoelectric performance. For example, Cr-doped PbSe (i.e., $\text{Pb}_{0.99}\text{Cr}_{0.01}\text{Se}$) exhibits a higher thermoelectric figure of merit (ZT) of ~ 1.7 at 2.8 GPa during the TCI transition at room-temperature conditions [16]. Hence, the discovery of new TCI materials and their fundamental understanding are very essential for technological applications. Further, it is important to highlight the uniqueness of the electronic band structure of ternary chalcogenide TIBiSe_2 . Upon increasing pressure, there is only one band inversion noticed at F point of the BZ while no overlap of energy bands near the Fermi level in the electronic band structure. Moreover, the experimentally observed TCI transition pressure (~ 2.5 GPa) is practically accessible by many available high-pressure techniques. Due to these fascinating features, the explored TCI transition in TIBiSe_2 can be potentially studied in detail by

many experimental techniques and unveil the mysteries of the TCI. Furthermore, our present and earlier study [13] confirm that the ternary chalcogenide family TlBiX_2 ($X = \text{S, Se, Te}$) are potential candidates to show the TCI transition. In these systems, the externally applied hydrostatic pressure acts as a switch to change its electronic topology. In specific, here the ambient condition 3D TI system TlBiSe_2 switches into TCI under hydrostatic pressure conditions at relatively lower pressure regions ~ 2.5 GPa. Finally, we hope that the discovered TCI phase in TlBiSe_2 will stimulate further high-pressure research interest in this class of materials using adequate quantum transport-sensitive measurements such as Shubnikov–de Haas oscillations, and optical measurements such as IR reflectivity for the complete fundamental understanding and possible technological applications.

VI. CONCLUSION

In conclusion, we comprehensively studied the hydrostatic pressure behavior of TlBiSe_2 using combined structural and vibrational spectroscopic experiments and first-principles DFT calculations. Structurally, the rhombohedral phase is stable up to ~ 7.0 GPa. However, observations of phonon (E_g) linewidth anomalies at ~ 2.5 GPa provide evidence for unusual electron-phonon coupling changes in the rhombohe-

dral phase of TlBiSe_2 . Further, the first-principles theoretical calculations corroborate the experimentally observed isostructural electronic transition as TCI transition marking a change in mirror Chern number n_M . The pressure-dependent evolution of the topological phases in the ternary chalcogenide family TlBiX_2 ($X = \text{S, Se, Te}$) exhibits a generic topological transition behavior with pressure. Finally, our studies suggest that the TI-based ternary chalcogenides (III-V-VI₂) constitute rich systems for the observation of topological phase transitions under hydrostatic pressure conditions.

ACKNOWLEDGMENTS

V.R., R.A., and S.R. gratefully acknowledge JNCASR for the research fellowship support. The high-pressure synchrotron XRD measurements at the Xpress beam line, Elettra synchrotron, Trieste, Italy were carried out with the help of financial support from the Department of Science and Technology (DST), Government of India, and therefore the authors sincerely thank DST. U.V.W. is thankful to the DST for support through a JC Bose national fellowship. We thank all the members of Light Scattering Lab, JNCASR, for their various help during this study. We acknowledge S. Janaky, and Dr. K. Kamali, JNCASR, for their help in the synchrotron.

-
- [1] M. Z. Hasan and C. L. Kane, *Rev. Mod. Phys.* **82**, 3045 (2010).
- [2] M. König, S. Wiedmann, C. Brüne, A. Roth, H. Buhmann, L. W. Molenkamp, X.-L. Qi, and S.-C. Zhang, *Science* **318**, 766 (2007).
- [3] D. Hsieh, Y. Xia, D. Qian, L. Wray, F. Meier, J. H. Dil, J. Osterwalder, L. Patthey, A. V. Fedorov, H. Lin, A. Bansil, D. Grauer, Y. S. Hor, R. J. Cava, and M. Z. Hasan, *Phys. Rev. Lett.* **103**, 146401 (2009).
- [4] Y. Xia, D. Qian, D. Hsieh, L. Wray, A. Pal, H. Lin, A. Bansil, D. Grauer, Y. S. Hor, R. J. Cava, and M. Z. Hasan, *Nat. Phys.* **5**, 398 (2009).
- [5] L. Fu, *Phys. Rev. Lett.* **106**, 106802 (2011).
- [6] J. C. Y. Teo, L. Fu, and C. L. Kane, *Phys. Rev. B* **78**, 045426 (2008).
- [7] M. S. Bahramy, B. J. Yang, R. Arita, and N. Nagaosa, *Nat. Commun.* **3**, 679 (2012).
- [8] X. Xi, C. Ma, Z. Liu, Z. Chen, W. Ku, H. Berger, C. Martin, D. B. Tanner, and G. L. Carr, *Phys. Rev. Lett.* **111**, 155701 (2013).
- [9] P. Dziawa, B. J. Kowalski, K. Dybko, R. Buczko, A. Szczerbakow, M. Szot, E. Łusakowska, T. Balasubramanian, B. M. Wojek, M. H. Berntsen, O. Tjernberg, and T. Story, *Nat. Mater.* **11**, 1023 (2012).
- [10] T. Sato, K. Segawa, K. Kosaka, S. Souma, K. Nakayama, K. Eto, T. Minami, Y. Ando, and T. Takahashi, *Nat. Phys.* **7**, 840 (2011).
- [11] V. Rajaji, F. J. Manjón, and C. Narayana, *J. Phys.: Condens. Matter* **34**, 423001 (2022).
- [12] V. Rajaji, U. Dutta, P. C. Sreeparvathy, S. C. Sarma, Y. A. Sorb, B. Joseph, S. Sahoo, S. C. Peter, V. Kanchana, and C. Narayana, *Phys. Rev. B* **97**, 085107 (2018).
- [13] V. Rajaji, R. Arora, S. C. Sarma, B. Joseph, S. C. Peter, U. V. Waghmare, and C. Narayana, *Phys. Rev. B* **99**, 184109 (2019).
- [14] A. Bera, K. Pal, D. V. S. Muthu, S. Sen, P. Guptasarma, U. V. Waghmare, and A. K. Sood, *Phys. Rev. Lett.* **110**, 107401 (2013).
- [15] A. Ohmura, Y. Higuchi, T. Ochiai, M. Kanou, F. Ishikawa, S. Nakano, A. Nakayama, Y. Yamada, and T. Sasagawa, *Phys. Rev. B* **95**, 125203 (2017).
- [16] L.-C. Chen, P.-Q. Chen, W.-J. Li, Q. Zhang, V. V. Struzhkin, A. F. Goncharov, Z. Ren, and X.-J. Chen, *Nat. Mater.* **18**, 1321 (2019).
- [17] Y. S. Ponomov, T. V. Kuznetsova, O. E. Tereshchenko, K. A. Kokh, and E. V. Chulkov, *JETP Lett.* **98**, 557 (2014).
- [18] S. N. Gupta, A. Singh, K. Pal, B. Chakraborti, D. V. S. Muthu, U. V. Waghmare, and A. K. Sood, *Phys. Rev. B* **96**, 094104 (2017).
- [19] K. Saha, K. Légaré, and I. Garate, *Phys. Rev. Lett.* **115**, 176405 (2015).
- [20] V. Rajaji, S. Janaky, S. C. Sarma, S. C. Peter, and C. Narayana, *J. Phys.: Condens. Matter* **31**, 165401 (2019).
- [21] J. Park, K.-H. Jin, Y. J. Jo, E. S. Choi, W. Kang, E. Kampert, J. S. Rhyee, S.-H. Jhi, and J. S. Kim, *Sci. Rep.* **5**, 15973 (2015).
- [22] P. P. Kong, F. Sun, L. Y. Xing, J. Zhu, S. J. Zhang, W. M. Li, Q. Q. Liu, X. C. Wang, S. M. Feng, X. H. Yu, J. L. Zhu, R. C. Yu, W. G. Yang, G. Y. Shen, Y. S. Zhao, R. Ahuja, H. K. Mao, and C. Q. Jin, *Sci. Rep.* **4**, 6679 (2014).
- [23] Y. L. Chen, Z. K. Liu, J. G. Analytis, J. H. Chu, H. J. Zhang, B. H. Yan, S. K. Mo, R. G. Moore, D. H. Lu, I. R. Fisher, S. C. Zhang, Z. Hussain, and Z. X. Shen, *Phys. Rev. Lett.* **105**, 266401 (2010).

- [24] O. Valassiades, E. K. Polychroniadis, J. Stoemenos, and N. A. Economou, *Phys. Status Solidi* **65**, 215 (1981).
- [25] O. Madelung, in *Semiconductors: Data Handbook*, edited by O. Madelung (Springer, Berlin, 2004), pp. 657.
- [26] K. Kuroda, M. Ye, A. Kimura, S. V. Eremeev, E. E. Krasovskii, E. V. Chulkov, Y. Ueda, K. Miyamoto, T. Okuda, K. Shimada, H. Namatame, and M. Taniguchi, *Phys. Rev. Lett.* **105**, 146801 (2010).
- [27] V. Rajaji, K. Pal, S. C. Sarma, B. Joseph, S. C. Peter, U. V. Waghmare, and C. Narayana, *Phys. Rev. B* **97**, 155158 (2018).
- [28] S. Klotz, J. C. Chervin, P. Munsch, and G. Le Marchand, *J. Phys. D: Appl. Phys.* **42**, 075413 (2009).
- [29] J. C. Chervin, B. Canny, and M. Mancinelli, *High Pressure Res.* **21**, 305 (2001).
- [30] A. P. Hammarsley, S. O. Svensson, M. Hanfland, A. N. Fitch, and D. Hausermann, *High Pressure Res.* **14**, 235 (1996).
- [31] J. Rodríguez-Carvajal, *Physica B* **192**, 55 (1993).
- [32] b. o. d.-f. t. Quantum-ESPRESSO is a community project for high-quality quantum-simulation software, and coordinated by P. Giannozzi. See <http://www.quantum-espresso.org>.
- [33] X. Hua, X. Chen, and W. A. Goddard, *Phys. Rev. B* **55**, 16103 (1997).
- [34] J. P. Perdew, K. Burke, and M. Ernzerhof, *Phys. Rev. Lett.* **77**, 3865 (1996).
- [35] G. Kresse and D. Joubert, *Phys. Rev. B* **59**, 1758 (1999).
- [36] A. Dal Corso, *Comput. Mater. Sci.* **95**, 337 (2014).
- [37] S. Baroni, S. de Gironcoli, A. Dal Corso, and P. Giannozzi, *Rev. Mod. Phys.* **73**, 515 (2001).
- [38] D. Gresch, G. Autès, O. V. Yazyev, M. Troyer, D. Vanderbilt, B. A. Bernevig, and A. A. Soluyanov, *Phys. Rev. B* **95**, 075146 (2017).
- [39] A. A. Soluyanov and D. Vanderbilt, *Phys. Rev. B* **83**, 235401 (2011).
- [40] J. Bhattacharjee and U. V. Waghmare, *Phys. Rev. B* **71**, 045106 (2005).
- [41] S. N. Toubektsis and E. K. Polychroniadis, *J. Cryst. Growth* **84**, 316 (1987).
- [42] K. Segawa, *Sci. Technol. Adv. Mater.* **16**, 014405 (2015).
- [43] See Supplemental Material at <http://link.aps.org/supplemental/10.1103/PhysRevB.107.205139> for the representative Le Bail fit to the synchrotron XRD patterns, additional discussion about N mode, Lorentzian fitting to the experimental Raman spectrum, DFT-calculated unit-cell parameters, theoretically calculated electronic structure of TlBiSe₂ without spin-orbit coupling, DFT-calculated pressure dependence of the Raman-active modes of TlBiSe₂, and theoretically calculated electronic structure of TlBiTe₂ with and without spin-orbit coupling. The Supplemental Material also contains Refs. [46–51,55].
- [44] F. D. Murnaghan, *Proc. Natl. Acad. Sci.* **30**, 244 (1944).
- [45] C. Bungaro and S. de Gironcoli, *Appl. Phys. Lett.* **76**, 2101 (2000).
- [46] <http://www.cryst.ehu.es>.
- [47] B. Hehlen, A. Amouri, A. Al-Zein, and H. Khemakhem, *J. Phys.: Condens. Matter* **26**, 015401 (2014).
- [48] R. A. Cowley, S. N. Gvasaliya, and B. Roesli, *Ferroelectrics* **378**, 53 (2009).
- [49] N. Dhifallah, B. Hehlen, and H. Khemakhem, *J. Raman Spectrosc.* **53**, 1148 (2022).
- [50] B. Hehlen and G. Simon, *J. Raman Spectrosc.* **43**, 1941 (2012).
- [51] G. Simon, B. Hehlen, R. Vacher, and E. Courtens, *Phys. Rev. B* **76**, 054210 (2007).
- [52] Y. A. Sorb, V. Rajaji, P. S. Malavi, U. Subbarao, P. Halappa, S. C. Peter, S. Karmakar, and C. Narayana, *J. Phys.: Condens. Matter* **28**, 015602 (2015).
- [53] R. S. Joshya, V. Rajaji, C. Narayana, A. Mascarenhas, and R. N. Kini, *J. Appl. Phys.* **119**, 205706 (2016).
- [54] M. Lazzeri, S. Piscanec, F. Mauri, A. C. Ferrari, and J. Robertson, *Phys. Rev. B* **73**, 155426 (2006).
- [55] I. Maria, R. Arora, M. Dutta, S. Roychowdhury, U. V. Waghmare, and K. Biswas, *J. Am. Chem. Soc.* **145**, 9292 (2023).
- [56] F. Giustino, *Rev. Mod. Phys.* **89**, 015003 (2017).